

ARTICLE OPEN



Extreme mechanical tunability in suspended MoS₂ resonator controlled by Joule heating

Anis Chiout¹, Cléophanie Brochard-Richard¹, Laetitia Marty², Nedjma Bendiab², Meng-Qiang Zhao^{3,4}, A. T. Charlie Johnson³, Fabrice Oehler¹, Abdelkarim Ouerghi¹ and Julien Chaste¹✉

Nanomechanical resonators are built into phones, as filters or accelerometers, but they lack a knob to effectively tune the frequency at the nanoscale when it's easy to tune on an octave the tone of a classical musical instrument like a guitar string. Moreover, the control of deformation in nanomaterials, as two-dimensional (2D) materials, to tailor their electronic properties, i.e., straintronic, opens up avenues for applications in force detection, bolometry or quantum emitters. An accurate control of the deformation within these materials is thus necessary to fully exploit their potential. The precise study of deformations in 2D materials involves measurements of vibration modes and nanomechanics. By using a suspended MoS₂ membrane heated by the Joule effect, we induce a strong softening of the mechanical resonance frequency as a function of the electrothermal heating, over one octave. A simple electrical tension is used to modulate the thermal mechanical tuning. Its amplitude is very large, greater than 100% modulation for one volt, compared to other approaches on 2D or 1D materials and, moreover, a very wide frequency range is accessible. Finally, we have related a photo-induced softening of the membrane over very long times with the current measurements and a photothermal effect.

npj 2D Materials and Applications (2023)7:20; <https://doi.org/10.1038/s41699-023-00383-3>

INTRODUCTION

The frequency of a musical instrument, such as a guitar string, is tunable over more than one octave, i.e., a ratio of two between the maximum and minimum frequency. It defines as $f_0 = \sqrt{\frac{k}{m}}$ in which k is the spring constant and m the resonator mass. To integrate successfully in devices or sensors, the resonator frequency must be tuned to the modes of the other components. When dimensions are reduced to nanometer sizes, such precise tuning is difficult to achieve in-situ. There is thus a demand for simple and robust techniques that can tune mechanical resonances at the nanoscale, and nano-resonators that can be tuned over a large frequency window. Among the different nano-resonators, carbon nanotube and two-dimensional (2D) materials have demonstrated the best performances for mechanical frequency tuning, including transition metal dichalcogenides (TMDs), 2D heterostructures^{1–12}, graphene^{13–39}, and nanotubes^{40–46}. We review more than 50 articles with different methods of modulating the frequency of vibration modes using a simple voltage. Some hold record for mass sensing⁴⁷ or force sensing^{13,48}, which makes them very desirable for applications or device, but none has yet achieved an efficient frequency adjustment over a large window, i.e., more than an octave.

When combined with 2D nanomechanics, thermal transport turns quite exciting, as materials with a large panel of thermal conductivities^{49,50} and extreme anisotropy⁵¹, are brought together with techniques to characterize their intrinsic properties⁵² and thermal measurements with a temperature sensitivity better than standard Raman spectroscopy techniques¹². It has also simple device applications, as shown by a single layer graphene membrane used fast bolometer (heat sensor) with a precision of the order of $\text{pW}\cdot\text{Hz}^{-0.5}$, comparable to the best current

detectors³³. It is worth noting that 2D materials have also radically altered our understanding of thermal transport at low dimensionality, proving that conventional models established for bulk crystals no longer apply at the nanoscale^{53–57}.

We design here a thermally-tuned nanomechanical resonator, which sits at the interface between heat transport in 2D materials and nanomechanics, with a focus on the electrothermal actuation of mechanical vibrations and their frequency tuning.

RESULTS

Experimental setup

We construct a nano-opto-electro-mechanical⁵² platform operating under vacuum (10^{-5} – 10^{-6} mbar) and at room temperature, to combine the electrical excitation and optical measurements of a suspended MoS₂ membrane. The sample consists of a pre-structured SiO₂ substrate with cavity and electrodes, covered by a few layers of MoS₂ deposited by 2D transfer technique^{58–60}. Figure 1a shows a schematic of the sample; the MoS₂ is contacted laterally with gold electrodes in order to apply a transverse DC source drain voltage (V_{ds}); the silicon (100) wafer is used as the back gate in a transistor configuration.

In the optical image, Fig. 1b, we see that the central cavity is fully covered by the MoS₂ monocrystal, so that the 2D material is suspended over the circular hole and forms a resonant drum. To confirm the flatness and the surface quality of our suspended membrane, we proceed to atomic force microscopy characterization in Fig. 1c. The typical vertical deflection of the membrane at rest position is below 1 nm. We excited electrically the drum movement and measure the vibration with a laser reflectometry (see methods). A typical resonance is shown in Fig. 1e near $f = 35$ MHz.

¹Université Paris-Saclay, CNRS, Centre de Nanosciences et de Nanotechnologies, 91120 Palaiseau, France. ²Univ. Grenoble Alpes, CNRS, Grenoble INP, Institut NÉEL, F-38000 Grenoble, France. ³Department of Physics and Astronomy, University of Pennsylvania, 2095 33rd Street, Philadelphia, PA 19104 6396, USA. ⁴Otto H. York Department of Chemical and Materials Engineering, New Jersey Institute of Technology, Newark, NJ 07102, USA. ✉email: julien.chaste@universite-paris-saclay.fr

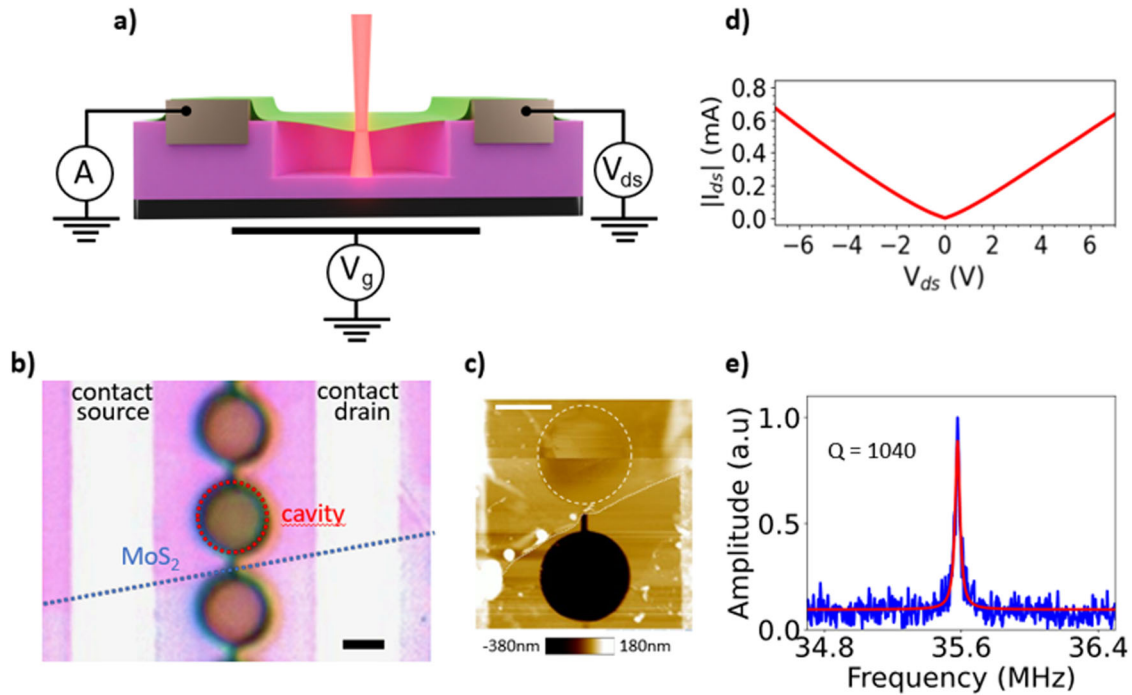


Fig. 1 Opto electromechanical setup. **a** Schematic of the suspended MoS₂ membrane in a back-gate transistor configuration, contacted laterally by two gold electrodes. **b** Optical microscopy image of the sample. Dotted lines are guide to the eye to locate the cavity and the MoS₂ crystal, scale bar is 2 μm. **c** Atomic force microscopy image of the suspended flake used for thermal measurements, scale bars is 2 μm. **d** Electrical characteristic $I_{ds}(V_{ds})$ of the sample **(e)** Mechanical response of the assembled membrane near 35.6 MHz, as measured by our optical technique. The quality factor at room temperature is $Q = 1040$.

From the literature, we know that the 2D material MoS₂ is a semiconductor with thickness-dependent properties, the band gap is indirect 1.3 eV in the bulk and changes to a direct band gap of 1.8 eV at the monolayer^{61,62}. Our red laser (633 nm, 1.96 eV), used for opto-mechanical monitoring, performs an above bandgap laser excitation in the material and the bulk of the charge carriers in our multilayer MoS₂ is thus photo-generated. Experimentally, the transverse electrical conductivity of the membrane strongly depends on the impinging laser power.

By measuring the lateral current I_{ds} against the corresponding voltage V_{ds} at a given laser power, we obtain The Joule heating of the membrane.

Here, our optomechanical measurements are typically carried out at $1.5 \cdot 10^4 \text{ W} \cdot \text{cm}^{-2}$ incident optical density (30 μW, spot size ~500 nm).

A highly tunable nano guitar

Mechanical resonators made of TMDs or 2D heterostructures have been shown to exhibit significant frequency tunability when varying electrical bias; generally only the gate voltage is considered¹⁻¹². In Fig. 2a, we plot the mechanical frequency f_0 as a function of the bias voltage for our MoS₂ resonator. The drum exhibits a huge tunability of the vibration frequency with respect to drain-source voltage V_{ds} , with a maximum frequency shift $\Delta f = f_{\max} - f_{\min}$ of 24 MHz, constructed from the maximum (f_{\max}) and minimum (f_{\min}) experimentally accessible. It is a tunability over 1.2 octave of the minimum frequency (10 MHz). Here f_{\max} is obtained at $V_{ds} = 0 \text{ V}$ while f_{\min} used $V_{ds} = 6 \text{ V}$ under a DC gate bias $V_g = 1 \text{ V}$.

The softening is related to the Joule heating of the membrane. The 2D drum can be heated locally, in the suspended part, for an applied electric power of a few mW. This has been confirmed by finite element analyses (see Supplementary Fig. 11) and, later on in the article, by Raman spectroscopy. To characterize the maximum of the frequency tuning efficiency (TE) for each

device, we define a figure of merit. The observed frequency tunability via source drain voltage $Tf_V = 1/f_0 \cdot (\partial f_0 / \partial V_{ds})_{\max}$ is huge in our experiment ($123\% \cdot \text{V}^{-1}$), for the maximum slope of $f_0(V_{ds})$ function with the applied bias. It is almost an order of magnitude greater than previous works see Fig. 2b-top¹⁻¹². on semiconducting (Fig. 2b, red-orange) and conducting (Fig. 2b, blue green) 2D materials. Only a single experimental report based on a graphene membrane obtained comparable electro-mechanical softening^{13,63}. There, the reported frequency shift was mainly obtained by an extreme capacitive force, created by a very short distance between the membrane and the metallic backgate (33–85 nm), close to the pull-in event. It remains difficult to achieve experimentally. High Tf_V was obtained for suspended carbon nanotubes in extreme conditions^{40,41}, this is due to the electron-phonon coupling inherent in low temperature measurements and high-quality samples with maximum tunability of only 1 MHz. Electrothermal actuation with high Tf_V of $30\% \cdot \text{V}^{-1}$ has already been reported with graphene membranes^{14,25}. This confirms the effectiveness of such a frequency adjustment method.

The absolute frequency tunability Tf_A , defined as $Tf_A = 2(f_{\max} - f_{\min}) / (f_{\max} + f_{\min})$ draws a similar picture, Fig. 2b-bottom. It defines the amplitude of the frequency range that is tunable, closely related to the dynamic range $DR = f_{\max} / f_{\min}$. We reached a value of 54%, it is among the best values reported so far. For all the devices studied, our work is the only one to have both a Tf_V and a Tf_A greater than 100%. To conclude, electrothermal actuation is a very simple and efficient way to adjust the frequency of a nanoresonator with a simple voltage.

DISCUSSION

In our case, the situation is different and we review in the following the contribution of each possible softening sources. For a clamped circular membrane, the frequency of the fundamental

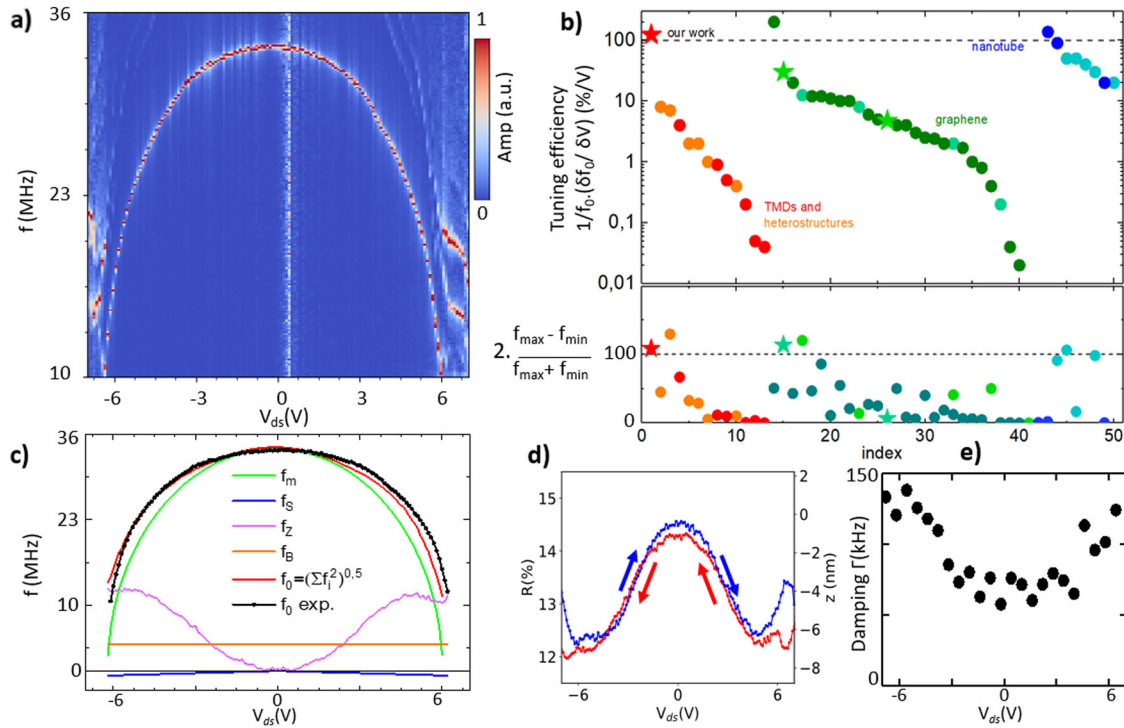


Fig. 2 Joule heating induced a tuning of the vibrations. **a** Variation of the frequency with respect to V_{ds} ($V_g = 1$ V). It shows a huge frequency tunability from 34 to 10 MHz for a V_{ds} variation of 7 V. A strong softening of the frequency is observed. **b** Values of the frequency tuning efficiency Tf_V and Tf_A for our work (index = 1) and other reference on TMDs and 2D heterostructures. **c** The experimental mode frequency and all different contributions f_m, f_s, f_z, f_B . **d** Reflectivity (R) and vertical deflection variation (Δz) of the sample with respect to V_{ds} ($V_g = 1$ V). The measurement is done at the middle of membrane. We arbitrarily fix $\Delta z = 0$ nm at $V_{ds} = 0$ V (red and blue for back and forth measurement). **e** The corresponding damping of the resonator $\Gamma = f_0/Q$.

mode f_0 decomposes as follows.

$$f_0 = \frac{1}{2\pi} \sqrt{f_m^2 + f_B^2 + f_z^2(z) - f_s^2(V_g)} \quad (1)$$

Each of the four major contributions is defined as⁵²

$$f_m^2 = \frac{2.405^2}{R^2} \sqrt{\frac{Y_0}{\rho t}} \quad (2)$$

$$f_B^2 \sim t^3 \quad (3)$$

$$f_z^2(z) = 2.405^2 \cdot 12/3 \cdot Et / (1 - \nu^2) \cdot z^2 / R^4 \rho \quad (4)$$

$$f_s^2(V_g) = 1.23 \epsilon_0 V_g^2 / d_0^3 \rho \quad (5)$$

The first term f_m^2 is strictly mechanical and detailed in Eq. (2). It links the in-plane mechanical tension (Y_0) to the geometrical considerations of the membrane (R , t its diameter and thickness, respectively) and to the material density (ρ). We notice that f_m is temperature dependant since the material dilatation will vary Y_0 as $Y_0(T)$. T is the membrane temperature profile convoluted by the mode shape. In our experiment, the membrane temperature T is mostly controlled by lateral electrothermal Joule heating between the drain and source contacts, with corresponding power $P_{ds} = I_{ds} \cdot V_{ds}$.

The second term f_B is detailed in Eq. (3) relates to the bending stiffness and is proportional to the cube of the membrane thickness t^3 . As our membrane is near atomically thin, $t = 5.8$ nm for five layers, f_B is neglected here, as in our previous work⁵².

The third term, $f_z(z)$ is detailed Eq. (4). It links the relative vertical displacement of the membrane center (z), measured against its rest position ($z_0 = 0$ at $V_{ds} = 0$ V in Fig. 2a), with the mechanical parameter Young Modulus (E) and the Poisson ratio (ν) of the 2D material, respectively. Here the vertical displacement includes the

deflection due to the static capacitive force F_C applied on the membrane and the photothermal forces or radiation pressure. We have $F_C = dC/dz \cdot (V_g - V_{ds}/2)^2$ in a diffusive and ohmic regime, with C the local capacitance.

The last term f_s is the contribution related to the capacitive softening and detailed in Eq. (4). It links the vacuum permittivity (ϵ_0) with the gate voltage (V_g) and the vertical distance (d_0) between the membrane rest position (z_0) to the bottom surface the cavity (i.e., “gate distance”). This last term can be estimated from the geometry of the device.

As f_z only depends on the (known) gate voltage V_g and the distance d_0 , we can quantify its magnitude by an independent determination of d_0 during the actual frequency measurements. To this end, we investigate in Fig. 2c, the variation of the laser reflectance (R) as a function the drain source voltage (V_{ds}) at a fixed gain voltage ($V_g = 1$ V). To exclude alternative softening source, we use a constant laser power (30 μ W) and the membrane is illuminated continuously for 30 min prior to the data acquisition to avoid any potential thermal drift induced by the laser. Modeling of 2D membrane and the underneath SiO_2 surface as a simple Fabry-Perot cavity, we obtain an expression of the absolute reflectance which depend on the actual length of the cavity ($d = d_0 + z$) and thus yields an in situ value of the membrane apex position (z), see Supplementary Fig. 12. We measure a maximum deflection $z = -6$ nm when a polarized lateral bias $V_{ds} = 6$ V is applied to the sample. Replacing this parameter in Eq. (4) we can evaluate the magnitude of f_z for this particular drain source voltage. Repeating this procedure for all individual V_{ds} , we deconvolve in Fig. 2d the contribution of f_z to the observed experimental variation. From the shape and the numerical variation, we see that the capacitive softening f_z is not the source of the observed strong mechanical softening with lateral bias. Other experiments varying the gate voltage (see Supplementary Fig. 8) confirms the previous conclusion.

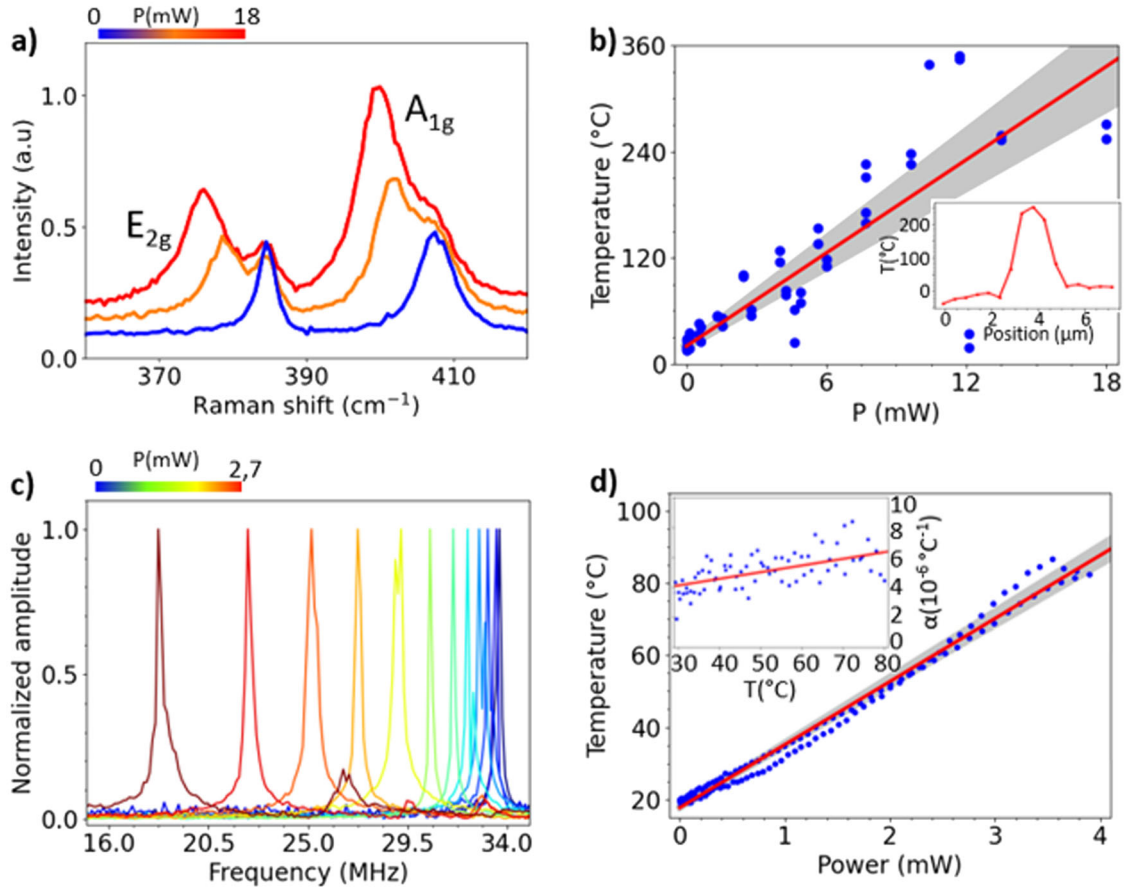


Fig. 3 Thermal transport measurement. **a** Raman spectroscopy of MoS₂ membrane at different joule heating power (P). Blue line: no bias applied, the membrane is not heated. Orange and red: we applied different source drain bias and achieved a heating power of $P = 8$ mW and $P = 19$ mW. **b** Temperature, obtained from Raman, of the 2D material in function of the applied power. The red line is a linear fit of the curve and the gray area the uncertainty of the slope. In inset, the spatial distribution of temperature measured by Raman during Joule Heating of 1 mW along a MoS₂ membrane center at 3.5 μm along the axis x . **c** Resonant frequency of MoS₂ membrane at different Joule heating power (P). Blue line: no bias applied, the membrane is not heated. from $P = 0$ mW to $P = 2.7$ mW ($V_g = 1$ V). **d** Temperature of the membrane in function of the applied power extracted from the mechanical resonance of the membrane. In inset, the extracted thermal expansion coefficient α in function of the temperature.

We can proceed similarly f_s and f_b , with similar conclusions, which leaves the f_m as the only possible source of the electromechanical tuning in our sample. Based on this hypothesis, we fit the experimental frequency shift (Fig. 2d, black dots) to obtain the experimental variation of f_m as a function of the drain source voltage (Fig. 2d, blue curve). As f_m only depends on V_{ds} via the thermal softening of the membrane in-plane tension γ_0 , we now have an experimental variation $\gamma_0(V_{ds}, I_{ds})$, which we can investigate against to the proper electrothermal heating model of our membrane by Joule effect (see in Supplementary Information). This strongly supports our hypothesis that Joule heating is the cause of membrane softening. This is confirmed also by Raman measurements, described later on.

To investigate experimentally the temperature profile of our membrane in-situ, during the optomechanical measurements, we turn to non-contact Raman spectroscopy. In Fig. 3a, the variations of two main Raman mode A_{1g} and E_{2g}^1 of the MoS₂ membrane are shown for different V_{ds} voltages. Without thermal heating (i.e. at room temperature), the reference position of the A_{1g} peak is 408 cm^{-1} and the E_{2g}^1 peak is 385 cm^{-1} . The two main Raman peaks A_{1g} and E_{2g}^1 are shifted with the electrical power applied to the sample by ΔA_{1g} and ΔE_{2g}^1 . The ratio of the two shift peaks being almost equal to 1, this is the signature of a temperature variation of the suspended membrane^{64,65}. Knowing the variation dA_{1g}/dT and dE_{2g}^1/dT are respectively $-0.016 \text{ cm}^{-1} \text{ K}^{-1}$ and $-0.013 \text{ cm}^{-1} \text{ K}^{-1}$,

and $-0.013 \text{ cm}^{-1} \text{ K}^{-1}$ and $-0.015 \text{ cm}^{-1} \text{ K}^{-1}$ for a multilayer⁶⁴, we compute the membrane temperature as follows: $T = 24^\circ\text{C} + \Delta E_{2g}^1 \cdot dE_{2g}^1/dT$. Proceeding similarly for all V_{ds} voltages, we combine in Fig. 3b the variation of Raman derived temperature and the experimental DC Joule heating ($P = I_{ds} V_{ds}$). The temperature of the membrane rises to 300 $^\circ\text{C}$ at $P = 18$ mW. We also observe a strong linear correlation, which we model (red line) as the direct heating of the membrane in vacuum. There are additional peaks in Fig. 3a. A fortiori, these extra peaks come from the unsuspended and thermalized part since the position does not change with heating. We assume here that the focalization is not optimized or that there is an artifact of the optical measurement. We have verified that a broader Gaussian laser distribution does not affect the simulated temperature too much (less than 10 $^\circ\text{C}$).

To this end, we consider a Comsol simulation of the Joule heating effect along the sample for applied power, see in see Supplementary Fig. 11 (temperature coupling and boundary electromagnetic heating modules). Our simulation needs to define a charge density profile along the device. In order to be accurate with our system. We consider that the current comes mainly from the photodoping and from the active traps which locally increase the doping and the charge density. The MoS₂ is suspended and under vacuum so no heat dissipation is possible in the out of plane direction and electrical energy is well converted into heat. We deduce the variation of the temperature compared to the

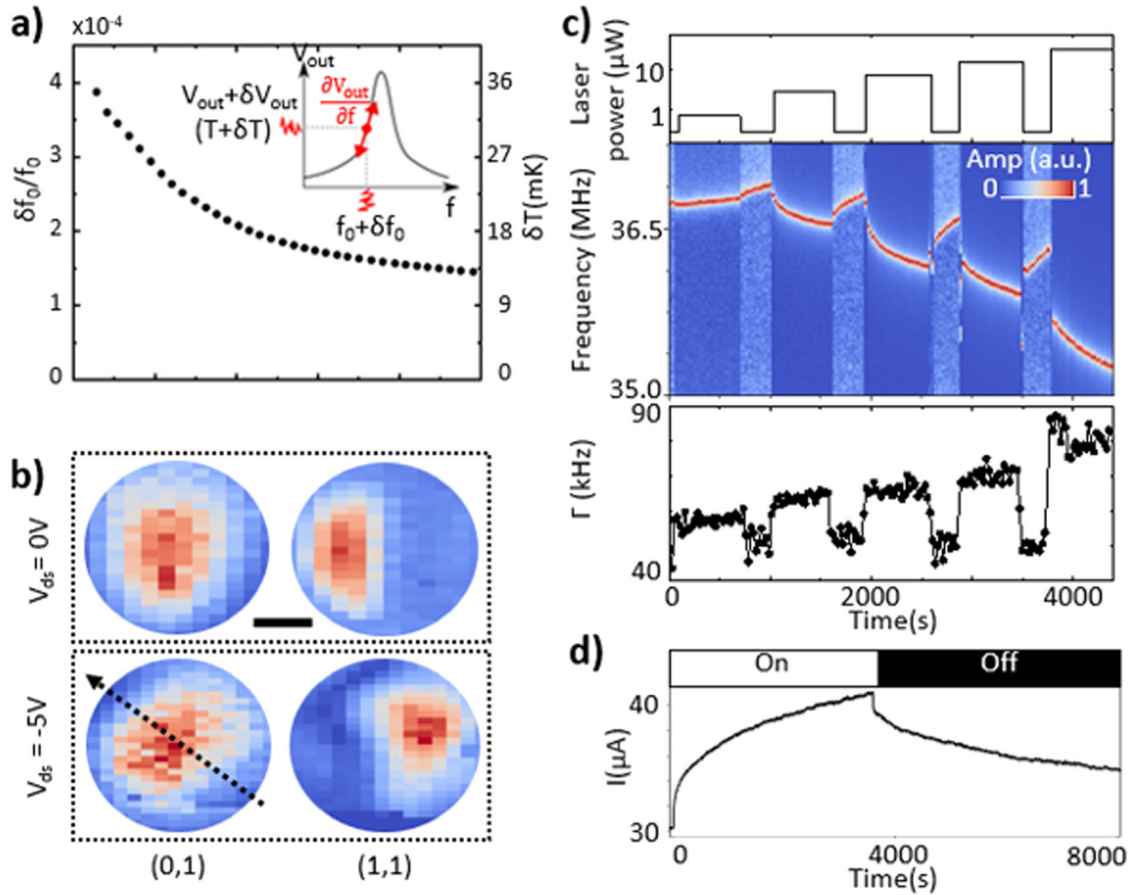


Fig. 4 Long living photothermal softening of the 2D membrane. **a** The Allan deviation of the mechanical resonance in function of the integration time, measured over a period of hundreds of seconds⁴⁷. In insert, a schematic to explain the measurement of frequency and temperature noise at mid amplitude along the mechanical response. **b** Spatial cartography of the two first mechanical modes of the drum at two different values of V_{ds} . The higher mode (1.1) is observed at high V_{ds} in (a). The field direction is indicated with the black dot arrow. Scale bar: 1 μm . **c** Measurement of the mechanical signal response and the damping rate Γ in function of time for different switching of the incoming laser power, from 300nW to 30 μW . For minimum power, at 300 nW, the response signal has been artificially enhanced for clarity. After some time without any light, the initial frequency is recovered. **d** Slow current variation over long time, $I_{ds}(t)$, when the laser is switch on and the laser is switch off.

calorific power of the membrane $dT/dP = 17.5 \text{ K.mW}^{-1}$. The resulting thermal conductivity k of the 2D material is $k = 50 \text{ W m}^{-1} \text{ K}^{-1}$ which corresponds to our previous report measured on similar MoS_2 and of typical values of thermal conductivity in suspended MoS_2 ⁶⁴.

We heat our sample with Joule heating and this results in strong mechanical softening with V_{ds} . There is an analogy between Raman spectroscopy measurements and the mechanical vibrations of our resonator regarding heat dependence and the temperature sensitivity^{12,33}. Having independently established the temperature variations of our MoS_2 membrane $T(V_{ds}/I_{ds})$ using Raman (Fig. 3b) and its mechanical softening $\gamma_0(V_{ds}, I_{ds})$ in Fig. 3c, we finally correlate in Fig. 3d those two quantities. At first order, we see that the frequency of the fundamental mode of the membrane is well described by a linear variation $\gamma_0(T) = \gamma_0 + \gamma_T(T)$ where γ_T is the additional tension due to the thermal dilatation at temperature T and $\gamma_0 = 0.7 \text{ N m}^{-1}$ the built-in tension at room temperature ($T_0 = 20^\circ\text{C}$). It is expressed as $\gamma_T = -Et \int_{T_0}^T \alpha(T') dT'$, α the thermal expansion coefficient (TEC). In first approximation, we neglect here any contribution from the underlying SiO_2 substrate and only consider the thermal expansion of the MoS_2 membrane. Using the Eq. (1), we can determine the total tension of the membrane at any heating power. Combining the Eq. (1) with our simulation of thermal conductivity, see in SI, we are able to extract the TEC for our material at each

heating power, in the inset of Fig. 3d. We obtain a TEC almost constant, as expected and around the value $\alpha = 5 \times 10^{-6} \text{ K}^{-1}$. It is in accordance to the value $\alpha = 4.9 \times 10^{-6} \text{ K}^{-1}$ obtained experimentally for bulk MoS_2 ^{66–69} and by theory^{70–73} and around $7 \times 10^{-6} \text{ K}^{-1}$ for monolayer MoS_2 . It corroborates our model of thermal heating. The slope for the variation of the mechanical vibration frequency is approximately $df_0/dP = 5.26 \text{ MHz.mW}^{-1}$. In order to extract the temperature sensitivity of our device, we fix the drive signal frequency at mid-amplitude of the mechanical resonance, that is to say when the response slope $\partial V_{out}/\partial f$ is maximum, and we measure the voltage output V_{out} for a long time. In Fig. 4a, we measured Allan's deviation of the frequency as a function of the integration time. We measured the output Voltage noise δV_{out} when the drive frequency is set at half the maximum amplitude of the resonance f_0 . The noise in temperature is $\delta T = \delta V_{out} \cdot (dT/df_0) \cdot (df_0/dV_{out})$. By converting the frequency noise, we get a temperature noise of $20 \text{ mK Hz}^{-0.5}$. By way of comparison, the temperature resolution with the Raman measurements is of the order of 20 K for a few seconds of integration per signal.

To confirm that our mechanical model is adequate to our system, we cartography the vertical displacement relative to two mechanical modes for different V_{ds} in Fig. 4b. The modes of a circular drum are Bessel functions of different orders, noted by their (m,n) index. The observed modes are the fundamental mode

($m = 0, n = 1$) which has a circular shape and the mode ($m = 1, n = 1$)^{74–76}. At $V_{ds} = 0$ V, the modes show the expected circular symmetry. When a lateral electrical field $V_{ds} = -5$ V is applied, the both modes are modified. We demonstrate the mode to be sensitive to the electric field in addition to the electrothermal softening since the temperature profile has a circular symmetry for a circular membrane, at less from the model.

Unlike electric heating, another strategy to address heat transport is to use local optical heating of 2D materials as with optomechanical studies^{12,77}, Raman spectroscopy^{50,78} or pump probe experiments^{56,79}. We have proceeded to measurement of the mechanical signal in function of time for different laser power, from 300 nW to 30 μ W, in Fig. 4c. With a power of 30 μ W, there is a strong softening of the vibration of 1.5 MHz and the damping rate increase from 50 kHz to 90 kHz. This photoinduced effect is highly similar to Joule heating experiment, in Figs. 2a and 2e, when a voltage around 3 V is applied to the resonator, the frequency decrease by almost 2 MHz and the damping increase from 60 kHz to 90 kHz. This similitude strongly suggests a photothermal heating of the membrane. The corresponding temperature increase is around 10 °C, which is also fully reasonable considering a laser power of few tens of μ W on a suspended 2D material.

We also measured the slow time response of the mechanical frequency, with a timescale above 500 s, in Fig. 4c and in the Supplementary Fig. 20. We previously reported such persistent mechanical softening effect (PPMS) of the mechanical resonance which has been related to long term persistent photocurrent (PPC) as it exists in our samples (Fig. 4d)^{52,80,81}. The PPC, as well as PPMS, results from charge traps located at the sulfur vacancies (S_V) along the sample. The origin of the long-time scale seems to lie in the large spatial separation of S_V traps and their random distribution and diffusion. It creates random potential energy for charge carriers. This phenomenon, and especially the timescale, is strongly temperature dependant^{80,81}. On contrary to PPC which are related to a strong photodoping of the 2D material, the mechanical counterpart PPMS is almost the same for different current I_{ds} or V_{ds} and not directly related to the charge flow (see Supplementary Fig. 19). In addition, as mention previously, we are able to quantify the doping effect with the mechanical capacitive terms $f_z^2(V_g)$ or $f_S^2(V_g)$. But the reflectance measurement has shown no out of plane deflection of the membrane, even few nanometer, during the long-time measurements. It means it is impossible to relate our slow mechanical softening measurement to any doping effect. Saying this, and since we suggest a photothermal heating for this very slow mechanical softening, our own interpretation consists to say that the phonons distribution and the local thermal conductivity is affected as well by the random potential energy and the diffusion of the S_V traps. It can explain the long-time term reduction of the vibration frequency but the absence of a direct relation with the doping and PPC.

To finish, we observe a damping increase by a factor 3 for high polarization, the temperature increases of 70 °C is not enough to explain this additional dissipation. Beyond the taking into account of the stationary local expansion of the material, which affect the mechanical frequency and the damping of our resonator, the heat propagation along the 2D material is at the origin of a response delay between the force and the movement. A light is absorbed by the 2D material and the material is mechanically deformed due to heating, after a certain delay time τ . In backaction, this deformation modifies the leakage of the photon population in the cavity. It defines the light-vibration coupling and the appearance of photothermal forces in micro and nanoresonators^{12,15,82,83}. It creates a drift $\Delta f = -f_0/2k \cdot \partial F/\partial z \cdot 1/(1 + (2\pi f_0 \tau)^2)$ and an additional damping $\Delta \Gamma = 4\pi f_0 \tau |\Delta f|$. This type of photo-induced force is proportional to the light reflection intensity at the z position and appearing when a native deflection is applied to the membrane¹². Deduced from the reflective measurements, the

out-of-plane deflection z induced a term $f_z(z)$ which is almost of the order of f_0 at high V_{DS} . This gives a time delay $\sigma \tau \sim \Delta \Gamma/4\pi f_0^2 \sim 3 \cdot 10^{-11}$ s for our measurements.

To conclude, we performed mechanical measurements on suspended MoS₂ membranes by combining optical reflection and electrical polarization. We heated the sample with an electrical current. The demonstration of the efficiency of Joule heating to tune mechanical resonance has been reported for our devices. We have compared the frequency tunability of vibrations by simple electric voltages, and the attainable frequency range, with many previous works and determined that the electrothermal method is very efficient and simpler than traditional capacitive methods or other solutions. Beyond that, the electrothermal tuning makes it possible to measure the thermal properties of the membrane such as thermal conductivity or thermal expansion of the material.

METHODS

Experimental set-up

We electrically drive the movement of the membrane using the AC gate bias (\tilde{V}_g)^{8,52} added to the DC back gate voltage (\overline{V}_g) so that the total back gate voltage is $V_g = \overline{V}_g + \tilde{V}_g$ ⁵². Optically, the MoS₂ membrane and the bottom Si surface of the cavity form a Fabry Perot interferometer^{8,84}, which converts the vertical displacement of the MoS₂ surface into modulations of the reflected intensity of the 633 nm laser (1.96 eV). This combination of electrical AC drive and optical detection allows one to scan the mechanical spectrum. The mechanical modulation of the laser reflection is the strongest when driving the membrane close to one of its resonant mechanical frequencies, see Fig. 1e near $f = 35$ MHz, which we characterize by its quality factor, $Q = 1040$ under vacuum (5×10^{-6} mbar), at room temperature.

$I_{ds}(V_{ds})$ curve are measured with Yokogawa sources and Femto current amplifier. We used a Long working distance objective $\times 100$ (Mitutoyo) for the reflectance and optomechanical measurements. A photodetector transduces the intensity of the reflected laser spot into voltage, which is recorded by a fast lock-in amplifier (Zurich instrument). Raman and PL spectroscopy was performed within the same vacuum chamber with a Horiba HR evolution system.

Sample fabrication and 2D transfer. Large sheets of MoS₂ are obtained by direct vapor deposition on silicon substrates. The transfer method consists, in a first step, in reducing the interaction between the 2D material and the substrate. For this, the substrate is covered with PMMA resin and immersed in liquid nitrogen, the difference in thermal expansion between 300 K and 77 K mechanically decoupling the different parts⁶⁰. The protective PMMA is then removed in acetone. The 2D sheets are then pick-up on PDMS/PPC bubbles using an HQ graphene transfer station. In order to increase the interaction forces between the bubble and the 2D, during the extraction of the 2D sheets, the capillary force of a drop of water is used during the transfer at the interface PPC/substrate⁵⁹. The sheets are then deposited on the pre-made structures over the etched holes in the SiO₂.

Supplementary material. In addition to the main manuscript, we provide all the details of Fig. 2b on the frequency tunability of 2D and 1D nanoresonators in the literature. We present the experimental setup, additional characterizations of the sample, and additional measurements of the Joule heating experiment. The Comsol simulation of the 2D heating is also detailed.

DATA AVAILABILITY

The data that support the findings of this study are available from the corresponding author upon reasonable request.

Received: 18 July 2022; Accepted: 10 March 2023;
Published online: 29 March 2023

REFERENCES

- Kumar, R. et al. Circular electromechanical resonators based on hexagonal-boron nitride-graphene heterostructures. *Appl. Phys. Lett.* **117**, 183103 (2020).
- Ye, F., Islam, A., Zhang, T. & Feng, P. X.-L. Ultrawide frequency tuning of atomic layer van der Waals heterostructure electromechanical resonators. *Nano Lett.* **21**, 5508–5515 (2021).
- Prasad, P., Arora, N. & Naik, A. K. Parametric amplification in MoS₂ drum resonator. *Nanoscale* **9**, 18299–18304 (2017).
- Šiškins, M. et al. Nanomechanical probing and strain tuning of the Curie temperature in suspended Cr₂Ge₂Te₆-based heterostructures. *npj 2D Materials and Applications* **6**, 41 (2022).
- Kim, S., Yu, J. & van der Zande, A. M. Nano-electromechanical drumhead resonators from two-dimensional material bimorphs. *Nano Lett.* **18**, 6686–6695 (2018).
- Will, M. et al. High quality factor graphene-based two-dimensional heterostructure mechanical resonator. *Nano Lett.* **17**, 5950–5955 (2017).
- Xie, H. et al. Tunable exciton-optomechanical coupling in suspended monolayer MoSe₂. *Nano Lett.* **21**, 2538–2543 (2021).
- Lee, J. et al. Electrically tunable single- and few-layer MoS₂ nanoelectromechanical systems with broad dynamic range. *Sci. Adv.* **4**, ea06653 (2018).
- Sengupta, S., Solanki, H. S., Singh, V., Dhara, S. & Deshmukh, M. M. Electro-mechanical resonators as probes of the charge density wave transition at the nanoscale in NbSe₂. *Phys. Rev. B* **82**, 155432 (2010).
- Morell, N. et al. High quality factor mechanical resonators based on WSe₂ monolayers. *Nano Lett.* **16**, 5102–5108 (2016).
- Kramer, E., van Dorp, J., van Leeuwen, R. & Venstra, W. J. Strain-dependent damping in nanomechanical resonators from thin MoS₂ crystals. *Appl. Phys. Lett.* **107**, 091903 (2015).
- Morell, N. et al. Optomechanical measurement of thermal transport in two-dimensional MoSe₂ lattices. *Nano Lett.* **19**, 3143–3150 (2019).
- Weber, P., Güttinger, J., Noury, A., Vergara-Cruz, J. & Bachtold, A. Force sensitivity of multilayer graphene optomechanical devices. *Nat. Commun.* **7**, 12496 (2016).
- Ye, F., Lee, J. & Feng, P. X.-L. Electrothermally tunable graphene resonators operating at very high temperature up to 1200 K. *Nano Lett.* **18**, 1678–1685 (2018).
- Barton, R. A. et al. Photothermal self-oscillation and laser cooling of graphene optomechanical systems. *Nano Lett.* **12**, 4681–4686 (2012).
- Guan, F., Kumaravadivel, P., Averin, D. V. & Du, X. Tuning strain in flexible graphene nanoelectromechanical resonators. *Appl. Phys. Lett.* **107**, 193102 (2015).
- Zhang, X. et al. Dynamically-enhanced strain in atomically thin resonators. *Nat. Commun.* **11**, 5526 (2020).
- Chen, C. et al. Performance of monolayer graphene nanomechanical resonators with electrical readout. *Nat. Nanotechnol.* **4**, 861–867 (2009).
- Güttinger, J. et al. Energy-dependent path of dissipation in nanomechanical resonators. *Nat. Nanotechnol.* **12**, 631–636 (2017).
- Luo, G. et al. Strong indirect coupling between graphene-based mechanical resonators via a phonon cavity. *Nat. Commun.* **9**, 383 (2018).
- Weber, P., Güttinger, J., Tsioutsios, I., Chang, D. E. & Bachtold, A. Coupling graphene mechanical resonators to superconducting microwave cavities. *Nano Lett.* **14**, 2854–2860 (2014).
- Davidovikj, D., Poot, M., Cartamil-Bueno, S. J., van der Zant, H. S. J. & Steeneken, P. G. On-chip heaters for tension tuning of graphene nanodrums. *Nano Lett.* **18**, 2852–2858 (2018).
- Parmar, M. M., Gangavarapu, P. R. Y. & Naik, A. K. Dynamic range tuning of graphene nanoresonators. *Appl. Phys. Lett.* **107**, 113108 (2015).
- Singh, V. et al. Probing thermal expansion of graphene and modal dispersion at low-temperature using graphene nanoelectromechanical systems resonators. *Nanotechnology* **21**, 165204 (2010).
- Ye, F., Lee, J. & Feng, P. X.-L. Very-wide electrothermal tuning of graphene nanoelectromechanical resonators. In: Proc. 30th IEEE International Conference on Micro Electro Mechanical Systems (MEMS) 68–71 (2017). <https://doi.org/10.1109/MEMSYS.2017.7863341>.
- Mathew, J. P., Patel, R. N., Borah, A., Vijay, R. & Deshmukh, M. M. Dynamical strong coupling and parametric amplification of mechanical modes of graphene drums. *Nat. Nanotechnol.* **11**, 747–751 (2016).
- Lee, S. et al. Electrically integrated SU-8 clamped graphene drum resonators for strain engineering. *Appl. Phys. Lett.* **102**, 153101 (2013).
- Singh, V. et al. Optomechanical coupling between a multilayer graphene mechanical resonator and a superconducting microwave cavity. *Nat. Nanotechnol.* **9**, 820–824 (2014).
- De Alba, R. et al. Tunable phonon-cavity coupling in graphene membranes. *Nat. Nanotechnol.* **11**, 741–746 (2016).
- Chen, C. et al. Graphene mechanical oscillators with tunable frequency. *Nat. Nanotechnol.* **8**, 923–927 (2013).
- Singh, R., Nicholl, R. J. T., Bolotin, K. I. & Ghosh, S. Motion transduction with thermo-mechanically squeezed graphene resonator modes. *Nano Lett.* **18**, 6719–6724 (2018).
- Luo, G. et al. Coupling graphene nanomechanical motion to a single-electron transistor. *Nanoscale* **9**, 5608–5614 (2017).
- Blaikie, A., Miller, D. & Alemán, B. J. A fast and sensitive room-temperature graphene nanomechanical bolometer. *Nat. Commun.* **10**, 4726 (2019).
- Xu, Y. et al. Radio frequency electrical transduction of graphene mechanical resonators. *Appl. Phys. Lett.* **97**, 243111 (2010).
- Miao, T., Yeom, S., Wang, P., Standley, B. & Bockrath, M. Graphene nanoelectromechanical systems as stochastic-frequency oscillators. *Nano Lett.* **14**, 2982–2987 (2014).
- Jung, M. et al. GHz nanomechanical resonator in an ultraclean suspended graphene p–n junction. *Nanoscale* **11**, 4355–4361 (2019).
- Descomin, A. et al. Giant, voltage tuned, quality factors of single wall carbon nanotubes and graphene at room temperature. *Nano Lett.* **19**, 1534–1538 (2019).
- Eichler, A. et al. Nonlinear damping in mechanical resonators made from carbon nanotubes and graphene. *Nat. Nanotechnol.* **6**, 339–342 (2011).
- Song, X. et al. Stamp transferred suspended graphene mechanical resonators for radio frequency electrical readout. *Nano Lett.* **12**, 198–202 (2012).
- Steele, G. A. et al. Strong coupling between single-electron tunneling and nanomechanical motion. *Science* **325**, 1103–1107 (2009).
- Benyamini, A., Hamo, A., Kusminskiy, S. V., von Oppen, F. & Ilani, S. Real-space tailoring of the electron-phonon coupling in ultraclean nanotube mechanical resonators. *Nat. Phys.* **10**, 151–156 (2014).
- Eichler, A., Ruiz, M., del Álamo, J. A. & Bachtold, A. Strong coupling between mechanical modes in a nanotube resonator. *Phys. Rev. Lett.* **109**, 025503 (2012).
- Sazonova, V. et al. A tunable carbon nanotube electromechanical oscillator. *Nature* **431**, 284–287 (2004).
- de Bonis, S. L. et al. Ultrasensitive displacement noise measurement of carbon nanotube mechanical resonators. *Nano Lett.* **18**, 5324–5328 (2018).
- Deng, G.-W. et al. Strongly coupled nanotube electromechanical resonators. *Nano Lett.* **16**, 5456–5462 (2016).
- Wen, Y. et al. A coherent nanomechanical oscillator driven by single-electron tunnelling. *Nat. Phys.* **16**, 75–82 (2020).
- Chaste, J. et al. A nanomechanical mass sensor with yoctogram resolution. *Nat. Nanotechnol.* **7**, 301–304 (2012).
- Moser, J. et al. Ultrasensitive force detection with a nanotube mechanical resonator. *Nat. Nanotechnol.* **8**, 493–496 (2013).
- Machida, Y., Matsumoto, N., Isono, T. & Behnia, K. Phonon hydrodynamics and ultrahigh-room-temperature thermal conductivity in thin graphite. *Science* **367**, 309–312 (2020).
- Majumdar, A., Chowdhury, S. & Ahuja, R. Ultralow thermal conductivity and high thermoelectric figure of merit in two-dimensional thallium selenide. *ACS Appl. Energy Mater.* **3**, 9315–9325 (2020).
- Vaziri, S. et al. Ultrahigh thermal isolation across heterogeneously layered two-dimensional materials. *Sci. Adv.* **5**, eaax1325 (2019).
- Chaste, J. et al. Phase transition in a memristive suspended MoS₂ monolayer probed by opto- and electro-mechanics. *ACS Nano* **14**, 13611–13618 (2020).
- Lee, S., Broid, D., Esfarjani, K. & Chen, G. Hydrodynamic phonon transport in suspended graphene. *Nat. Commun.* **6**, 6290 (2015).
- Cepellotti, A. et al. Phonon hydrodynamics in two-dimensional materials. *Nat. Commun.* **6**, 6400 (2015).
- Fugallo, G. et al. Thermal conductivity of graphene and graphite: collective excitations and mean free paths. *Nano letters* **14**, 6109–6114 (2014).
- Huberman, S. et al. Observation of second sound in graphite at temperatures above 100 K. *Science* **364**, 375–379 (2019).
- Ding, Z. et al. Phonon hydrodynamic heat conduction and Knudsen minimum in graphite. *Nano Lett.* **18**, 638–649 (2018).
- Henck, H. et al. Electrolytic phototransistor based on graphene-MoS₂ van der Waals p-n heterojunction with tunable photoresponse. *Appl. Phys. Lett.* **109**, 113103 (2016).
- Ma, X. et al. Capillary-force-assisted clean-stamp transfer of two-dimensional materials. *Nano Lett.* **17**, 6961–6967 (2017).
- Wang, P. et al. High-fidelity transfer of chemical vapor deposition grown 2D transition metal dichalcogenides via substrate decoupling and polymer/small molecule composite. *ACS Nano* (2020) <https://doi.org/10.1021/acsnano.0c02838>.
- Mak, K. F., Lee, C., Hone, J., Shan, J. & Heinz, T. F. Atomically thin MoS₂ a new direct-gap semiconductor. *Phys. Rev. Lett.* **105**, 136805 (2010).
- Kuc, A., Zibouche, N. & Heine, T. Influence of quantum confinement on the electronic structure of the transition metal sulfide TS₂. *Phys. Rev. B* **83**, 245213 (2011).
- Sillanpää, M. A., Khan, R., Heikkilä, T. T. & Hakonen, P. J. Macroscopic quantum tunneling in nanoelectromechanical systems. *Phys. Rev. B* **84**, 195433 (2011).

64. Chaste, J. et al. Intrinsic properties of suspended MoS₂ on SiO₂/Si pillar arrays for nanomechanics and optics. *ACS Nano* **12**, 3235–3242 (2018).
65. Lee, J. E., Ahn, G., Shim, J., Lee, Y. S. & Ryu, S. Optical separation of mechanical strain from charge doping in graphene. *Nat. Commun.* **3**, 1024 (2012).
66. Lin, Z. et al. Thermal expansion coefficient of few-layer MoS₂ studied by temperature-dependent Raman spectroscopy. *Sci. Rep.* **11**, 7037 (2021).
67. Hu, X. et al. Mapping thermal expansion coefficients in freestanding 2D materials at the nanometer scale. *Phys. Rev. Lett.* **120**, 055902 (2018).
68. Murray, R. & Evans, B. The thermal expansion of 2H-MoS₂ and 2H-WSe₂ between 10 and 320 K. *J. Appl. Crystallogr.* **12**, 312–315 (1979).
69. Zhang, L. et al. Thermal expansion coefficient of monolayer molybdenum disulfide using micro-Raman spectroscopy. *Nano Lett.* **19**, 4745–4751 (2019).
70. Sevik, C. Assessment on lattice thermal properties of two-dimensional honeycomb structures: graphene, hBN, hMoS₂, and hMoSe₂. *Phys. Rev. B* **89**, 035422 (2014).
71. Gan, C. K. & Liu, Y. F. Direct calculation of the linear thermal expansion coefficients of MoS₂ via symmetry-preserving deformations. *Phys. Rev. B* **94**, 134303 (2016).
72. Wang, Z.-Y. et al. Effects of in-plane stiffness and charge transfer on thermal expansion of monolayer transition metal dichalcogenide. *Chin. Phys. B* **24**, 026501 (2015).
73. Huang, L. F. Correlation between structure, phonon spectra, thermal expansion, and thermomechanics of single-layer MoS₂. *Phys. Rev. B* **90**, 045409 (2014).
74. Davidovikj, D. et al. Visualizing the motion of graphene nanodrums. *Nano Lett.* **16**, 2768–2773 (2016).
75. Wang, Z. et al. Resolving and tuning mechanical anisotropy in black phosphorus via nanomechanical multimode resonance spectromicroscopy. *Nano Lett.* **16**, 5394–5400 (2016).
76. Yuan, X. et al. A frequency-tunable nanomembrane mechanical oscillator with embedded quantum dots. *Appl. Phys. Lett.* **115**, 181902 (2019).
77. Liu, C.-H., Kim, I. S. & Lauhon, L. J. Optical control of mechanical mode-coupling within a mos₂ resonator in the strong-coupling regime. *Nano Lett.* **15**, 6727–6731 (2015).
78. Balandin, A. A. et al. Superior thermal conductivity of single-layer graphene. *Nano Lett.* **8**, 902–907 (2008).
79. Kim, S. E. et al. Extremely anisotropic van der Waals thermal conductors. *Nature* **597**, 660–665 (2021).
80. Chandan, Sarkar, S. & Angadi, B. Defects induced persistent photoconductivity in monolayer MoS₂. *Appl. Phys. Lett.* **118**, 172105 (2021).
81. George, A. et al. Giant persistent photoconductivity in monolayer MoS₂ field-effect transistors. *npj 2D Mater. Appl.* **5**, 1–8 (2021).
82. Metzger, C. H. & Karrai, K. Cavity cooling of a microlever. *Nature* **432**, 1002–1005 (2004).
83. Metzger, C., Favero, I., Ortlieb, A. & Karrai, K. Optical self cooling of a deformable Fabry-Perot cavity in the classical limit. *Phys. Rev. B* **78**, 035309 (2008).
84. Wang, Z. & Feng, P. X.-L. Interferometric motion detection in atomic layer 2D nanostructures: visualizing signal transduction efficiency and optimization pathways. *Sci. Rep.* **6**, 28923 (2016).

ACKNOWLEDGEMENTS

The work was supported by French grants ANR ANETHUM (ANR-19-CE24-0021), ANR Deus-nano (ANR-19-CE42-0005), ANR 2DHeco (ANR-20-CE05-0045) and by

the French Renatech network. A.T.C.J. acknowledges support from the National Science Foundation MRSEC DMR-1720530. This work was partially financially supported by the Indo-French Centre for the Promotion of Advanced Research (CEFIPRA, Project No. 6008-1).

AUTHOR CONTRIBUTIONS

A.O., F.O., and J.C. conceived the experiments. A.C. performed the Joule heating and laser interferometry measurements. M.Q.Z. and A.T.C.J. synthesized and characterized the MoS₂ crystals. A.C., C.B.R., A.O., F.O., and J.C. fabricated the samples, developed the 2D transfer technique and performed the Raman spectroscopy measurements. A.C., J.C., L.M., and N.B. analyzed and proposed a model to fit the experimental data. J.C. supervised the project. The paper was jointly written by all authors. All authors discussed the results and commented on the paper.

COMPETING INTERESTS

The authors declare no competing financial or non-financial interests.

ADDITIONAL INFORMATION

Supplementary information The online version contains supplementary material available at <https://doi.org/10.1038/s41699-023-00383-3>.

Correspondence and requests for materials should be addressed to Julien Chaste.

Reprints and permission information is available at <http://www.nature.com/reprints>

Publisher's note Springer Nature remains neutral with regard to jurisdictional claims in published maps and institutional affiliations.



Open Access This article is licensed under a Creative Commons Attribution 4.0 International License, which permits use, sharing, adaptation, distribution and reproduction in any medium or format, as long as you give appropriate credit to the original author(s) and the source, provide a link to the Creative Commons license, and indicate if changes were made. The images or other third party material in this article are included in the article's Creative Commons license, unless indicated otherwise in a credit line to the material. If material is not included in the article's Creative Commons license and your intended use is not permitted by statutory regulation or exceeds the permitted use, you will need to obtain permission directly from the copyright holder. To view a copy of this license, visit <http://creativecommons.org/licenses/by/4.0/>.

© The Author(s) 2023